Journal of Power Sources 246 (2014) 198–203

Contents lists available at ScienceDirect

Journal of Power Sources

journal homepage: www.elsevier.com/locate/jpowsour

Three-dimensionally porous Fe_3O_4 as high-performance anode materials for lithium–ion batteries

Hao Wu, Ning Du, Jiazheng Wang, Hui Zhang, Deren Yang*

State Key Lab of Silicon Materials, Department of Materials Science and Engineering, Cyrus Tang Center for Sensor Materials and Applications, Zhejiang University, Hangzhou 310027, People's Republic of China

HIGHLIGHTS

- Fe_3O_4 layer was deposited on a Cu 3D porous current collector.
- The porous Fe_3O_4 electrodes show superior cyclability and rate capabilities.
- Enhanced performance is attributed to the advantages of the porous structure.

ARTICLE INFO

Article history:
Received 20 May 2013
Received in revised form
10 July 2013
Accepted 12 July 2013
Available online 20 July 2013

Keywords:
Iron oxide
Three-dimensional
Porous electrodes
Lithium–ion batteries

ABSTRACT

This paper describes the synthesis of three-dimensionally porous Fe_3O_4 via template-assisted and subsequent electrochemical deposition methods. When used as anode materials of lithium–ion batteries, the porous Fe_3O_4 electrodes show better cyclability and enhanced rate capabilities compared to planar Fe_3O_4 electrodes. The superior performance can be attributed to improved electrical contact, fast electron transport and good strain accommodation of the porous electrodes. The effect of the thickness of the porous Fe_3O_4 electrodes on the lithium–ion battery performance has also been investigated.

1. Introduction

Rechargeable lithium–ion batteries (LIBs) have been the most utilized power source for portable electronic devices [1,2]. Graphite-based materials are commonly used as anode materials in most commercial LIBs due to their low cost, high yield and long cycle life. However, their limited gravimetric capacity (372 mAh g^{-1}) has prompted intensive research for alternative anode materials with large capacity at low potentials for next-generation vehicles [3]. Since the discovery of transition metal oxides as anode materials of LIBs, much effort has been devoted to improve their capacity and rate capability [4–6]. In contrast to the intercalation mechanism, transition metal oxides show a reversible "conversion process" in which the transition metal oxides are reduced to small metal clusters which can facilitate the decomposition of Li_2O [4–6]. Among the transition metal oxides, Fe_3O_4 (magnetite) is cheap, nontoxic and environmentally benign, which is considered as one of the most promising electrode materials [5,7]. The electrochemical evaluation results have shown that Fe_3O_4 reacts with eight Li ions per formula unit with a theoretical specific capacity of ~926 mAh g^{-1} which is far beyond that of commercial graphite anodes [8–10]. Furthermore, Fe_3O_4 exhibits higher electronic conductivities compared with other transition metal oxides.

Nevertheless, application of Fe_3O_4-based materials in practical LIBs is hindered due to its low rate capability arising from kinetic limitations and poor cycling stability owing to severe agglomerations and drastic volume change during Li–ion insertion and extraction [5]. Various strategies have been pursued for the synthesis of Fe_3O_4 nanostructures to circumvent the above-mentioned obstacles and achieve enhanced electrochemical performance. For example, Taberna et al. prepared a self-supported Fe_3O_4/Cu nanoarchitectured electrode for LIBs, which delivered good rate capability [5]. Zhang and co-workers reported the carbon-coated Fe_3O_4 nanospindles synthesized by partial reduction of hematite nanospindles with high reversible capacity (~745 mAh g^{-1} at C/5) as well as enhanced cycling performance [11]. Wang et al. fabricated

* Corresponding author. Tel.: +86 571 87953190; fax: +86 571 87952322.
E-mail address: mseyang@zju.edu.cn (D. Yang).

0378-7753/$ – see front matter © 2013 Published by Elsevier B.V.
http://dx.doi.org/10.1016/j.jpowsour.2013.07.063

graphene-encapsulated Fe_3O_4 nanoparticles with 3D laminated structure, which exhibited a stable capacity of about 650 mAh g^{-1} with no noticeable fading for up to 100 cycles [12]. For all these studies, the improved electrochemical performances can be attributed to efficient buffering of volume change, fast electron transport and good electrical contact during cycling.

More recently, we demonstrated a new type of 3D nano-architectured porous Cu via a simple template-assisted method, which can support the Si-based materials to improve their cycling performance [13]. Herein, we apply the porous Cu to deposit Fe_3O_4 as anode materials of LIBs, which delivers excellent cyclability and enhanced rate capabilities compared to planar Fe_3O_4 electrodes. The effect of the thickness of the Fe_3O_4 on the performance has also been investigated.

2. Experimental section

2.1. Synthesis of the porous Fe_3O_4 electrodes

The synthesis of porous Cu structure is similar to our previous paper with small modification [13]. Briefly, monodispersed silica spheres were synthesized by a modified Stöber method [14]. Then, 500 μL of as-prepared silica–ethanol solution was dispersed on a pre-cleaned Cu substrate, which was subsequently spin-coated at 1000 rpm for 30 s. The thickness of this layer can be varied by repeating the spin-coating steps. The as-grown silica opal-like templates were annealed at 100 °C for 2 h under a low pressure before electrochemical deposition of Cu. The inverse-opal-like Cu current collector was achieved by cathodic electrodeposition from an electrolytic bath consisting of $CuSO_4 \cdot 5H_2O$ 100 g L^{-1}, $(NH_4)_2SO_4$ 20 g L^{-1}, diethylenetriamine (DETA) 40 mL L^{-1}, into the interstices between the piled silica nanospheres of the above-mentioned templates, with a LK2006A electrochemical work station. The electrodeposition of Cu was carried out under galvanostatic conditions at a constant current density of −3 mA cm^{-2}. After deposition for 5 min, the silica–Cu composites were then converted to copper inverse-opal-like current collector by chemically etching the silica in aqueous HF solution (10 wt%) for 30 min. The copper 3D nanoporous network was deposited with Fe_3O_4 by another electrodeposition process from an alkaline aqueous solution consisting of 0.09 M $Fe_2(SO_4)_3$, 2 M NaOH complexed with 0.1 M triethanolamine. The magnetite coating was produced under stirring at a constant current density ($j = -5$ mA cm^{-2}) using the same three-electrode cell as-described above at a fixed temperature of 50 °C. Four types of thickness-controlled electrodes were prepared for comparison by depositing time of 30, 60, 90 and 120 s, respectively.

2.2. Characterization and electrochemical measurement

The obtained samples were characterized by X-ray powder diffraction (XRD) with a Rigaku D/max-ga X-ray diffractometer with graphite monochromatized Cu Kα radiation ($\lambda = 1.54178$ Å). The morphology and structure of the samples were examined by a field emission scanning electron microscope (SEM HITACH S4800) with an energy-dispersive X-ray spectrometer (EDX).

Electrochemical measurements were performed by coin type cells (CR2025) which were assembled in an argon-filled glove box (Mbraun, labstar, Germany) by directly using the as-synthesized porous Fe_3O_4 structures as the positive electrode, a lithium metal foil as the negative electrode, and 1 M $LiPF_6$ electrolyte solution (in EC:DMC/1:1 in volume ratio). A galvanostatic cycling test of the assembled cells was carried out on a Land CT2001A system within the potential range of 0.01–3.0 V at various discharge/charge current densities. Cyclic voltammetry (CV) was conducted in the potential window of 0.01–3.0 V and a scan rate of 0.1 mV s^{-1} on an Arbin BT 2000 system.

3. Results and discussion

As shown in Fig. 1, the fabrication of the porous Fe_3O_4 electrodes involves three steps: 1) growth of silica opal-like templates on a Cu substrate; 2) Cu inverse-opal-like porous current collector synthesized by electrodeposition of Cu in the interstices of silica nanospheres and subsequent removal of templates by HF etching; 3) deposition of a Fe_3O_4 layer onto the porous copper structure via another electrodeposition.

Fig. 2 shows the morphological and compositional characterization of a porous Fe_3O_4 electrode deposited for 60 s. It can be seen that the as-synthesized Cu substrate shows the ordered porous structure of uniformly distributed holes with a diameter of ~200 nm (Fig. 2a). After the deposition of Fe_3O_4, most of the holes have been covered by a uniform layer and the diameters of the holes decrease (Fig. 2b). Fig. 2c shows the cross-sectional SEM image of the porous Fe_3O_4 electrode. As observed, not only the surface holes, but also the inner holes were injected by Fe_3O_4 due to the uniform electrodeposition which is different from the sputtering deposition [13]. Energy–dispersive X-ray (EDX) spectroscopy was carried out to verify the composition of the as-synthesized sample (Fig. 2d). Elements Cu, Fe and O are detected, which may come from the Cu current collector and Fe_3O_4 layer, respectively. Fig. 3 shows the XRD pattern of the as-synthesized sample, in which all peaks are consistent with those of the Fe_3O_4 phase (JCPDS No. 19-0629) in addition to the reflections owing to metallic copper, further confirming the deposition of Fe_3O_4 layer.

The CV curve of a 60 s deposition time porous Fe_3O_4 electrode is shown in Fig. 4a. The sharp peak located at about 0.7 V in the first discharge curve can be attributed to the conversion of Fe_3O_4 to Fe and the formation of amorphous Li_2O ($Fe_3O_4 + 8Li^+ + 8e^- \leftrightarrow 3Fe^0 + 4Li_2O$) as well as the irreversible reaction with electrolyte [12,15]. Meanwhile, two peaks at about 1.63 and 1.86 V are recorded in the anodic process, corresponding to the reversible oxidation of Fe^0 to Fe^{3+} [16]. In the subsequent cycles, both reduction and oxidation peaks are positively shifted. The difference in the potential of the cathodic peaks between the second and the first cycle is due to the structural modification of Fe_3O_4 and also the strain introduced in Fe_3O_4 during the first cycle caused by the lithium insertion and extraction [17,18]. On the other hand, the positive shift of the anodic peaks is ascribed to the polarization of the electrode in the first cycle [15]. Moreover, peak

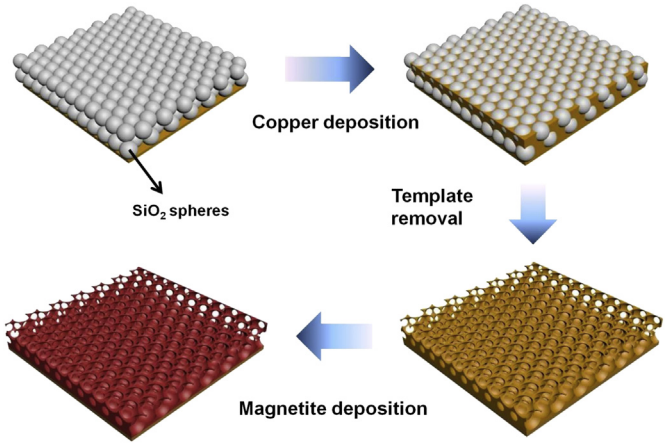

Fig. 1. Schematic of the fabrication process for porous Fe_3O_4 electrodes.

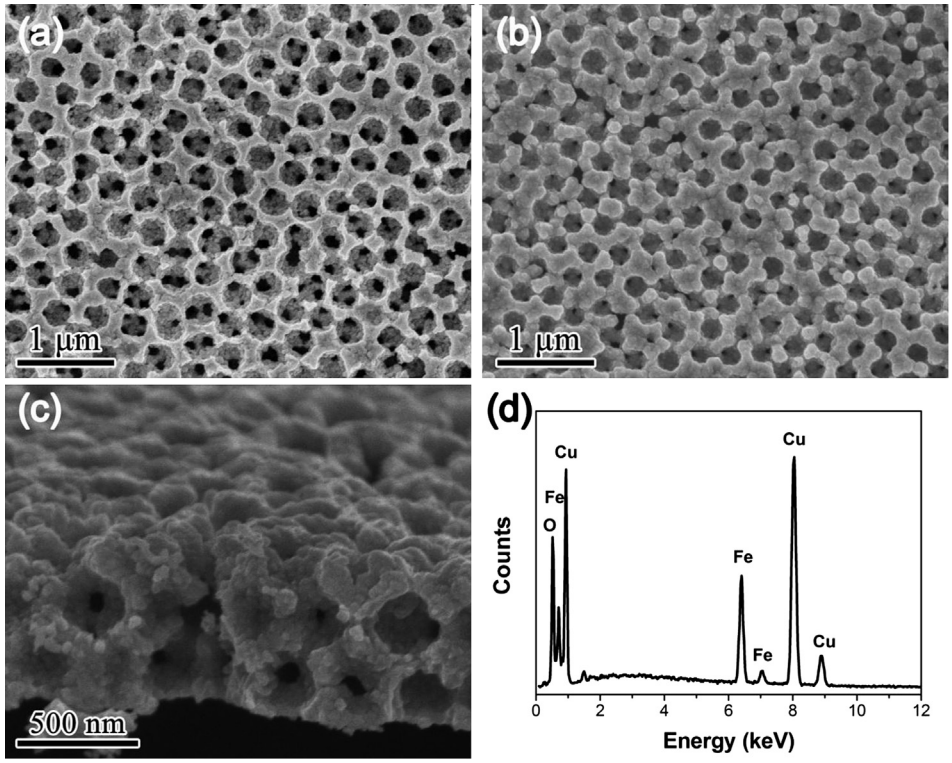

Fig. 2. (a) SEM image of a porous Cu current collector; (b) top view and (c) cross-sectional view of the porous Fe_3O_4 electrodes deposited for 60 s; (d) EDX spectrum of the porous Fe_3O_4 electrodes.

current density and integrated area intensity are nearly unchanged in the following cycles, indicating the good cycling performance. The porous Fe_3O_4 electrode was first cycled at 1 A g^{-1} in 0.01–3.0 V. Fig. 4b shows 1st, 2nd, 3rd, 10th and 20th charge and discharge curves. In the first discharge/charge curve, the well-defined potential plateaus at about 0.8/1.6 V versus Li^+/Li are observed, which are close to that described in the literature for Fe_3O_4 anodes [5,19]. The first discharge and charge capacity is found to be ~1308 mAh g^{-1} and 983 mAh g^{-1}, respectively, leading to an initial columbic efficiency of ~75%. The irreversible capacity loss in the first cycle can be attributed to the formation of a solid electrolyte interphase film (SEI) and electrolyte decomposition. The initial irreversible capacity loss may be decreased by

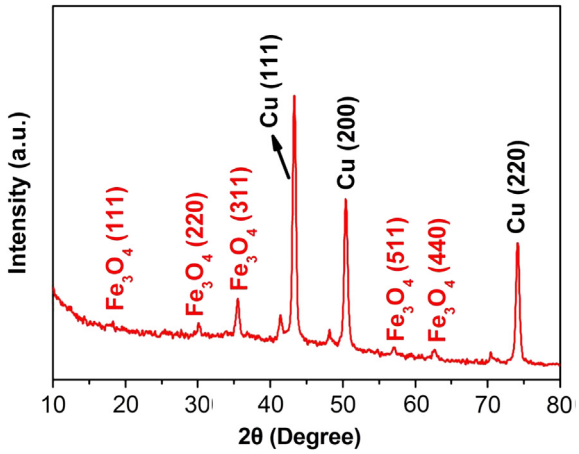

Fig. 3. XRD pattern of Fe_3O_4 electrodeposited onto porous Cu current collector.

further coating of carbon layer on the Fe_3O_4. Nevertheless, after the initial two cycles, the columbic efficiency increases to above 98%, indicating the high reversibility in the subsequent cycles. The subsequent discharge/charge curves of these corresponding cycles mostly overlap, indicating the capacity remains unchanged. To further investigate the cycling stability of the porous Fe_3O_4 electrodes, the capacity versus cycle numbers were investigated at 1 A g^{-1}. As observed, the porous Fe_3O_4 electrodes maintains high reversibility and its reversible capacity even gradually increases to 1382 mAh g^{-1} after 100 cycles. The rise in capacity is not surprising for the nanostructured transition metal oxide electrode, which can be attributed to the reversible growth of a polymeric gel-like film resulting from kinetically activated electrolyte degradation [20–22]. In contrast, the capacity of the bare Fe_3O_4 electrode deposited (60 s) directly on a Cu planar substrate continuously deteriorates and only ~34% of the initial capacity can be retained after 30 cycles, indicating the poor cycling performance. The porous structure allows for good accommodation of the volume change, large surface area contact with active materials and good conductivity, which should be responsible for the enhanced performance.

The rate capability of the porous and planar electrode is demonstrated in Fig. 4d and e. It can be seen that the porous electrode shows a capacity of 1030 mAh g^{-1} at 0.5 A g^{-1} and it changes to 1033, 1034, 1014, 1002 and 960 mAh g^{-1} with the current density increases to 1, 2, 4, 8 and 16 A g^{-1}. When the current restores to 0.5 A g^{-1}, a capacity of 1310 mAh g^{-1} is retained, which is even much higher than the initial value, further confirming the high reversibility of the porous electrode. However, the capacity of the planar electrode drops dramatically with less than 11% of the initial value after 60 cycles, indicating the advantage of the porous electrode. We also tested the durability of the porous electrode at high rates. It can be seen from Fig. 4e that a capacity of 1180, 1054,

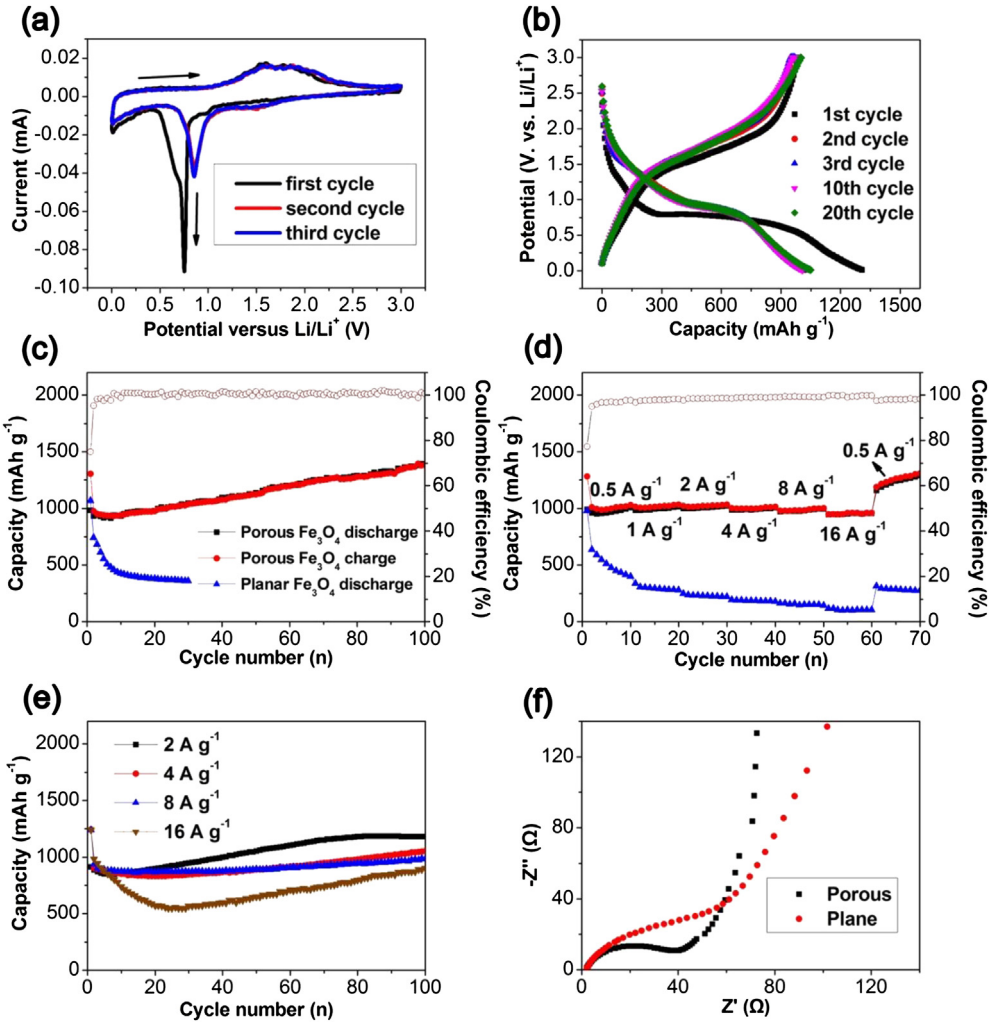

Fig. 4. (a) Cyclic voltammograms for the as-prepared porous Fe_3O_4 electrodes (60 s deposition time) between 3.0 V and 0.01 V versus Li/Li^+ at a scan rate of 0.1 mV s^{-1}; (b) galvanostatic charge/discharge profiles plotted for the 1st, 2nd, 3rd, 10th and 20th cycles at 1 A g^{-1}; (c) cycling performance of porous Fe_3O_4 electrodes at current density of 1 A g^{-1} and (d) rate performance of planar Fe_3O_4 electrode and porous Fe_3O_4 electrode; (e) discharge capacities of the porous Fe_3O_4 electrodes at current densities of 2, 4, 8 and 16 A g^{-1}, respectively; (f) impedance measurements of planar electrode and porous Fe_3O_4 electrode.

984 and 900 mAh g^{-1} can be obtained after 100 cycles at current densities of 2, 4, 8 and 16 A g^{-1}, respectively. To the best of our knowledge, the rate capability of the porous Fe_3O_4 electrodes is superior to the previous data [5,7,23–25]. The superior electrochemical performance, in terms of cycling stability and rate capability, can be ascribed to the porous structure that can prevent agglomeration, accommodate large volume expansion, avoid the cracking and pulverization of the electrode, and enhance the electron and lithium−ions conduction. The electrochemical impedance spectra of the porous and planar Fe_3O_4 electrodes were also measured to provide further insights. The Nyquist plots in Fig. 4f for the above two electrodes show a straight line in the low frequency region and a depressed semicircle in the high frequency region. The intercept on the Z real axis in the high frequency range indicates the resistance of the electrolyte (R_s). The high frequency semicircle is related to the SEI film and/or contact resistance (R_{SEI}) and the middle frequency semicircle represents the charge-transfer resistance (R_{ct}) through the electrode/electrolyte interface. The inclined line in the low frequency region corresponds to the Warburg impedance (Z_W) during the solid state lithium-diffusion process in the electrode materials [26,27]. No significant difference can be observed between the diameters of semicircles in the high frequency region for both electrodes. However, the impedance response of the porous electrodes exhibits a smaller semicircle in the middle frequency region, suggesting lower charge-transfer resistance (R_{ct}). Consequently, improved conductivity of the porous Cu/Fe_3O_4 electrodes as demonstrated by the impedance curves results in enhanced cycling performance of the cells during charge-discharge process.

The effects of the thickness of Fe_3O_4 film on the electrochemical performance were investigated to optimize the deposition parameters. Fig. 5 shows the SEM images of the as-prepared porous Fe_3O_4 electrodes with different deposition time ranging from 30 to 120 s. At the initial stage of the film growth, small and shapeless polycrystalline Fe_3O_4 grains cover the entire surface of the Cu current collector as shown in Fig. 5a. Then, with increasing deposition time, the Fe_3O_4 coating layer becomes thicker, resulting in the shrinkage of the void space in the porous electrodes (Fig. 5b–d). The porous Fe_3O_4 electrodes with different thicknesses were characterized for their cycling performance at a constant current density of 2 A g^{-1}. Fig. 6 exhibits the cycling performance for the four as-described porous Fe_3O_4 electrodes. The corresponding mass loading of Fe_3O_4 is measured to be 0.061, 0.102, 0.150 and 0.225 mg cm^{-2}, corresponding to different deposition time of 30, 60, 90 and 120 s,

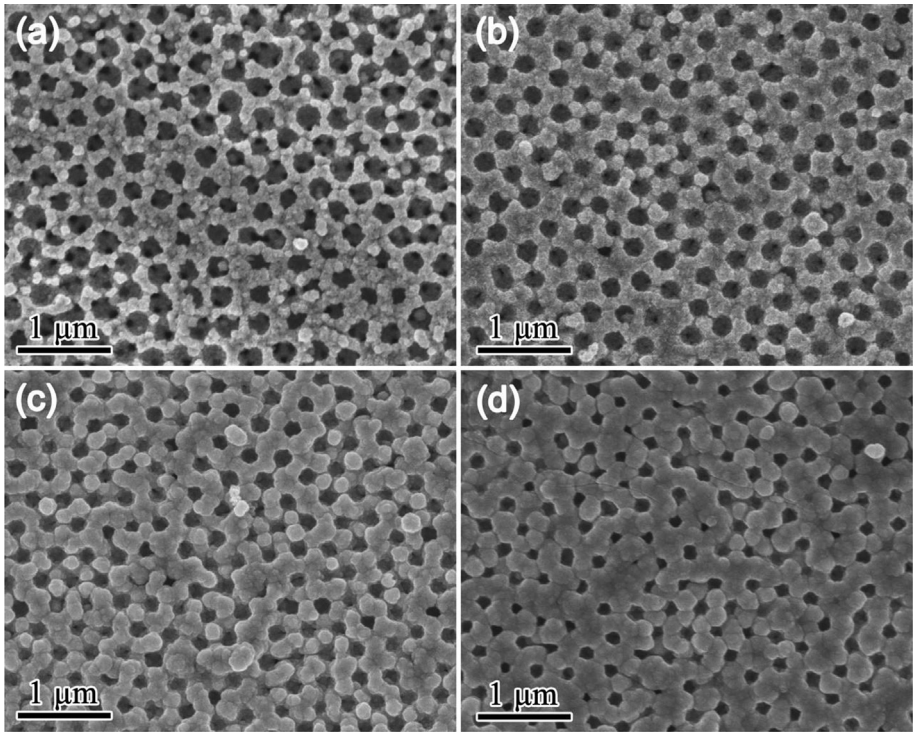

Fig. 5. SEM images of the porous Fe_3O_4 electrodes with varied thickness of Fe_3O_4 layer with different deposition time: (a) 30 s; (b) 60 s; (c) 90 s; (d) 120 s, respectively.

respectively. All the four electrodes show excellent cycling stability due to the above-mentioned advantages of the 3D porous nanostructures. Similar electrochemical behavior of these electrodes suggests that the thickness of Fe_3O_4 film has no obvious or significant effect on the specific gravimetric capacity. Nevertheless, there is a slight decrease of discharge capacities as the deposition time increases. In other words, electrodes with shorter lithium–ion diffusion length, which is inherent to thinner Fe_3O_4 film (e.g. 30 s deposition time), exhibit better cycling performance. Meanwhile, discharge capacities of the electrodes with thicker Fe_3O_4 film (e.g. 120 s deposition time) deteriorates in comparison with less active materials as excessive Fe_3O_4 particles may block the electrolyte accessibility to the interstices in the porous network, resulting in insufficient void space to buffer the volume change during cycling.

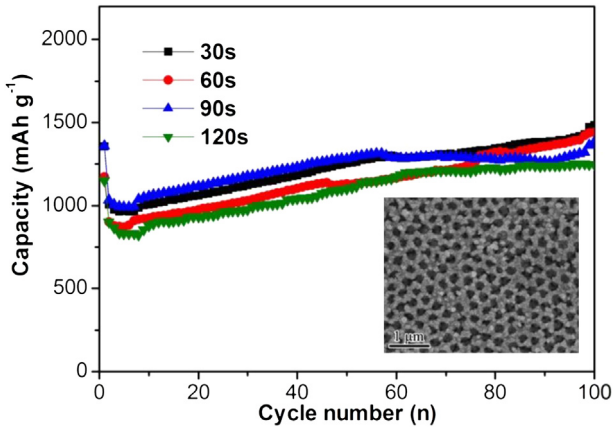

Fig. 6. Discharge capacities of the porous Fe_3O_4 electrodes with four different thickness of Fe_3O_4 layer, the inset shows the SEM image of the electrode (30 s deposition time) after 20 cycles at current density of 2 A g^{-1}.

The inset SEM image reveals the morphology of porous Fe_3O_4 electrode (30 s deposition time) after 20 cycles at a current density of 2 A g^{-1}, which shows no peeling or other morphological changes, further confirming the chemical and mechanical robustness of the porous electrodes.

4. Conclusion

In summary, porous Fe_3O_4 structure on a Cu substrate was synthesized by electrochemically depositing the Fe_3O_4 film for 60 s on a pre-prepared porous Cu current collector. When utilized as anode materials for LIBs, the porous Fe_3O_4 electrodes delivered a reversible capacity of 1382 mAh g^{-1} after 100 cycles at a current density of 1 A g^{-1}. The porous electrode shows a capacity of 1030 mAh g^{-1} at 0.5 A g^{-1} and it changes to 1033, 1034, 1014, 1002 and 960 mAh g^{-1} with the current density increases to 1, 2, 4, 8 and 16 A g^{-1}. When the current restores to 0.5 A g^{-1}, a capacity of 1310 mAh g^{-1} is retained. The enhanced electrochemical performance can be attributed to improved electrical contact, fast electron transport and good strain accommodation of the porous electrode.

Acknowledgments

The authors would like to appreciate the financial supports from the 863 Project (No. 2011AA050517), NSFC (No. 51002133), Innovation Team Project of Zhejiang Province (2009R50005), and Fundamental Research Funds for the central Universities.

References

[1] M. Armand, J.M. Tarascon, Nature 451 (2008) 652–657.
[2] J. Tollefson, Nature 456 (2008) 436–440.
[3] C.K. Chan, X.F. Zhang, Y. Cui, Nano Lett. 8 (2008) 307–309.
[4] P. Poizot, S. Laruelle, S. Grugeon, L. Dupont, J.M. Tarascon, Nature 407 (2000) 496–499.

[5] P.L. Taberna, S. Mitra, P. Poizot, P. Simon, J.-M. Tarascon, Nat. Mater. 5 (2006) 567–573.
[6] S.H. Lee, Y.H. Kim, R. Deshpande, P.A. Parilla, E. Whitney, D.T. Gillaspie, K.M. Jones, A.H. Mahan, S.B. Zhang, A.C. Dillon, Adv. Mater. 20 (2008) 3627–3632.
[7] S. Mitra, P. Poizot, A. Finke, J.M. Tarascon, Adv. Funct. Mater. 16 (2006) 2281–2287.
[8] P.C. Lian, X.F. Zhu, H.F. Xiang, Z. Li, W.S. Yang, H.H. Wang, Electrochim. Acta 56 (2010) 834–840.
[9] L. Wang, Y. Yu, P.C. Chen, D.W. Zhang, C.H. Chen, J. Power Sources 183 (2008) 717–723.
[10] Z.M. Cui, L.Y. Jiang, W.G. Song, Y.G. Guo, Chem. Mater. 21 (2009) 1162–1166.
[11] W.M. Zhang, X.L. Wu, J.S. Hu, Y.G. Guo, L.J. Wan, Adv. Funct. Mater. 18 (2008) 3941–3946.
[12] J.Z. Wang, C. Zhong, D. Wexler, N.H. Ldris, Z.X. Wang, L.Q. Chen, H.K. Liu, Chem. Eur. J. 17 (2011) 661–667.
[13] J.Z. Wang, N. Du, Z.Q. Song, H. Wu, H. Zhang, D.R. Yang, J. Power Sources 229 (2013) 185–189.
[14] W. Stöber, A. Fink, E. Bohn, J. Colloid Interface Sci. 26 (1968) 62–69.
[15] L. Ji, Z. Tan, T.R. Kuykendall, S. Aloni, S. Xun, E. Lin, V. Battaglia, Y. Zhang, Phys. Chem. Chem. Phys. 13 (2011) 7170–7177.
[16] Y. He, L. Huang, J.S. Cai, X.M. Zheng, S.G. Sun, Electrochim. Acta 55 (2010) 1140–1144.
[17] M.Y. Li, Y. Wang, C.L. Liu, H. Gao, W.S. Dong, Electrochim. Acta 67 (2012) 187–193.
[18] P. Wang, M.X. Gao, H.G. Pan, J.L. Zhang, C. Liang, J.H. Wang, P. Zhou, Y.F. Liu, J. Power Sources 239 (2013) 466–474.
[19] G.M. Zhou, D.W. Wang, F. Li, L.L. Zhang, N. Li, Z.S. Wu, L. Wen, G.Q. Lu, H.M. Cheng, Chem. Mater. 22 (2010) 5306–5313.
[20] S. Laruelle, S. Grugeon, P. Poizot, D.S. Molle, L. Dupont, J.-M. Tarascon, J. Electrochem. Soc. 149 (2002) A627–A634.
[21] S. Grugeon, S. Laruelle, L. Dupont, J.M. Tarascon, Solid State Sci. 5 (2003) 895–904.
[22] J.S. Do, C.H. Weng, J. Power Sources 146 (2005) 482–486.
[23] C. Ban, Z. Wu, D.T. Gillaspie, L. Chen, Y. Yan, J.L. Blackburn, A.C. Dillon, Adv. Mater. 22 (2010) E145–E149.
[24] M.L. Sanchez, A. Primo, H. Garcia, J. Mater. Chem. 22 (2012) 21373–21375.
[25] T. Muraliganth, A.V. Murugan, A. Manthiram, Chem. Commun. (2009) 7360–7362.
[26] Y. Li, J. Li, J. Phys. Chem. C 112 (2008) 14216–14219.
[27] J. Wang, J. Chen, K. Konstantinov, L. Zhao, S.H. Ng, G.X. Wang, Z.P. Guo, H.K. Liu, Electrochim. Acta 51 (2006) 4634–4638.